Grain-size distribution in the mantle wedge of subduction zones

Ikuko Wada,[1] Mark D. Behn,[2] and Jiangheng He[2]

Received 7 February 2011; revised 14 July 2011; accepted 23 July 2011; published 20 October 2011.

[1] Mineral grain size plays an important role in controlling many processes in the mantle wedge of subduction zones, including mantle flow and fluid migration. To investigate the grain-size distribution in the mantle wedge, we coupled a two-dimensional (2-D) steady state finite element thermal and mantle-flow model with a laboratory-derived grain-size evolution model. In our coupled model, the mantle wedge has a composite olivine rheology that incorporates grain-size-dependent diffusion creep and grain-size-independent dislocation creep. Our results show that all subduction settings lead to a characteristic grain-size distribution, in which grain size increases from 10 to 100 μm at the most trenchward part of the creeping region to a few centimeters in the subarc mantle. Despite the large variation in grain size, its effect on the mantle rheology and flow is very small, as >90% of the deformation in the flowing part of the creeping region is accommodated by grain-size-independent dislocation creep. The predicted grain-size distribution leads to a downdip increase in permeability by ~5 orders of magnitude. This increase is likely to promote greater upward migration of aqueous fluids and melts where the slab reaches ~100 km depth compared with shallower depths, potentially providing an explanation for the relatively uniform subarc slab depth. Seismic attenuation derived from the predicted grain-size distribution and thermal field is consistent with the observed seismic structure in the mantle wedge at many subduction zones, without requiring a significant contribution by the presence of melt.

Citation: Wada, I., M. D. Behn, and J. He (2011), Grain-size distribution in the mantle wedge of subduction zones, *J. Geophys. Res.*, *116*, B10203, doi:10.1029/2011JB008294.

1. Introduction

[2] Many processes in the mantle wedge, such as mantle flow, the migration of aqueous fluids and melts, and the attenuation of seismic waves, depend on mineral grain size (Figure 1). For example, at a relatively high temperature in the upper mantle, grain size determines the relative importance of the two main deformation mechanisms, diffusion and dislocation creeps [e.g., *Karato and Wu*, 1993], which in turn affect mantle rheology and mantle wedge flow. Grain size also influences grain-scale permeability and the migration of aqueous fluids and melts in the mantle wedge [e.g., *Hirth and Kohlstedt*, 2003; *Wark et al.*, 2003]. Furthermore, grain size affects the attenuation of seismic waves and thus the interpretation of observed seismic structures [e.g., *Jackson et al.*, 2002; *Faul and Jackson*, 2005; *Behn et al.*, 2009]. Therefore, understanding the distribution of grain size is critical to the study of the mantle wedge geodynamics.

[3] In earlier studies on the evolution of grain size [e.g., *Twiss*, 1977; *Karato et al.*, 1980; *Ross et al.*, 1980; *Van der Wal et al.*, 1993], grain size was directly related to stress and was used as a paleopiezometer. However, more recent studies indicate that grain size is also sensitive to temperature and strain rate [e.g., *De Bresser et al.*, 1998, 2001; *Hall and Parmentier*, 2003; *Montési and Hirth*, 2003; *Austin and Evans*, 2007]. Based on microstructural observations of the evolution of grain size during laboratory experiments, grain-size evolution at the relatively high temperatures of the upper mantle is related to two competing processes, static grain growth and dynamic recrystallization [*Karato*, 1984]. Static grain growth occurs through grain boundary migration driven by reduction of total interfacial energy [e.g., *Urai et al.*, 1986; *Karato*, 1989; *Evans et al.*, 2001]. Dynamic recrystallization occurs through reconfiguration of crystalline defects driven by reduction of stored energy associated with the defects and results in grain-size reduction [e.g., *Twiss*, 1977; *Karato et al.*, 1980; *Ross et al.*, 1980; *Van der Wal et al.*, 1993]. Grain-size evolution models that include static grain growth and dynamic recrystallization explicitly incorporate the temperature and strain rate dependence of these two mechanisms [e.g., *Hall and Parmentier*, 2003; *Austin and Evans*, 2007].

[4] Another proposed theory for grain-size evolution is based on damage theories [e.g., *Bercovici and Ricard*, 2005; *Ricard and Bercovici*, 2009], in which the generation of grain boundaries occurs because of the imposed deformation field as in the dynamic recrystallization theory. Whether the dynamic recrystallization and damage theories are reconcilable has yet to be investigated. Phase transformation can

[1]Department of Geology and Geophysics, Woods Hole Oceanographic Institution, Woods Hole, Massachusetts, USA.
[2]Pacific Geoscience Centre, Geological Survey of Canada, Sidney, British Columbia, Canada.

0148-0227/11/2011JB008294

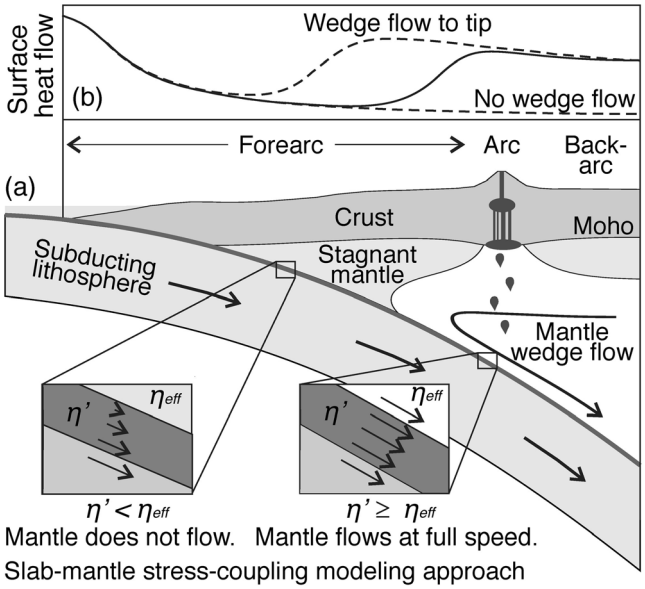

Figure 1. (a) Schematic diagram of a typical subduction zone with a relatively young and warm subducting slab along a continental margin and (b) the corresponding surface heat flow. Insets in 1a show how the effect of slab-mantle (de)coupling is modeled by using a thin layer along the plate interface in our model. The strength contrast between the interface layer (η') and mantle (η_{eff}) controls the slab-mantle coupling.

also influence grain size as a grain of a new phase nucleate and grows at the expense of an old phase [*Aaronson*, 1993]. This mechanism has been applied to explain the rheology of the subducting slab [e.g., *Riedel and Karato*, 1997] and the lower mantle [e.g., *Solomatov et al.*, 2002], but its effect on grain size in the mantle wedge is likely minimal because no phase transformation of the main constituent mineral of the upper mantle, olivine, is expected to occur in this region.

[5] In the mantle wedge, the thermal and deformation conditions are expected to vary significantly over relatively short distances [e.g., *Kincaid and Sacks*, 1997; *van Keken et al.*, 2002; *Kelemen et al.*, 2003; *Wada et al.*, 2008], and thus a large variation in grain size is expected. Grain size in mantle xenoliths, such as those from continental extension zones [e.g., *Avé Lallemant et al.*, 1980], subarc upper mantle [*Blatter and Carmichael*, 1998] and kimberlites in stable cratons [e.g., *Kopylova et al.*, 1999], ranges from a few microns in ultramylonites formed in localized shear zones to a few centimeters. In the mantle wedge, given the wide range of thermal and deformation conditions, a comparable variation in grain size of up to 4 orders of magnitude can be expected. Such a large variation can have a significant influence on the physical state of the mantle wedge.

[6] In this study, we explore the distribution of grain size in the mantle wedge by coupling a two-dimensional (2-D) steady state thermal and mantle-flow model with the grain-size evolution model of *Austin and Evans* [2007]. In the model, we use a composite mantle rheology that accounts for grain-size-dependent diffusion creep and grain-size-independent dislocation creep. Thus, the resulting deformation and thermal fields not only affect grain size but also depend on grain size, resulting in nonlinear feedback between the two fields and grain size. The coupled model calculates the three variable fields that are in equilibrium with one another. Using this approach, we map the distribution of grain size in the wedge for a range of subduction settings and investigate the variability of the grain-size distribution and its implications for grain-scale permeability, fluid and melt migration, and seismic attenuation in the mantle wedge.

2. Modeling Approach

2.1. Steady State Grain-Size Model

[7] In this paper, we consider laboratory-derived grain-size evolution (GSE) models that are based on the theories of static grain growth and dynamic recrystallization. Among those, two models proposed by *Austin and Evans* [2007] (hereafter referred to as the *A&E*) and *Hall and Parmentier* [2003] were previously tested against the experimental data of *Behn et al.* [2009]. Although the difference in the two models is arguably small compared with the uncertainties associated with extrapolating the laboratory data to the upper mantle conditions, the tests conducted by *Behn et al.* [2009] showed a better fit of the *A&E* GSE model to the experimental data.

[8] We couple the *A&E* GSE model with a mantle-flow model parameterized for wet olivine, assuming a water content of 1000 H/10^6 Si [*Hirth and Kohlstedt*, 2003; *Behn et al.*, 2009]. The *A&E* GSE model assumes that static grain growth and dynamic recrystallization operate independently, and the rate of change in grain size ($\dot{d}$) is equal to the sum of the rates of the two processes:

$$\dot{d} = \left[\frac{G_0}{p_g}\exp\left(-\frac{E_g + PV_g}{RT}\right)d^{1-p_g}\right] + \left[-\frac{\chi\sigma\dot{\varepsilon}_{disl}}{c\gamma}d^2\right], \quad (1)$$

where d is the grain size, G_0 is the grain growth rate constant, p_g is the grain growth constant, E_g and V_g are the grain growth activation enthalpy and volume, respectively, P is confining pressure, R is the universal gas constant (8.3145 J mol^{-1} K^{-1}), T is absolute temperature, χ is the fraction of the work done by dislocation creep associated with changing grain boundary area, σ is the shear stress; $\dot{\varepsilon}_{disl}$ is the strain rate of dislocation creep, c is a geometric constant, and γ is the average specific grain boundary energy [*Austin and Evans*, 2007; *Behn et al.*, 2009]. The parameter values are given in Table 1. The first and second terms on the right-hand side describe the rates of static grain growth and dynamic recrystallization, respectively. The negative sign in the second term indicates that dynamic recrystallization results in grain-size reduction. When the rates of the two mechanisms are balanced, grain size achieves a steady state value (d_{ss}):

$$d_{ss} = \left(\frac{G_0 c\gamma\exp\left(-\frac{E_g + PV_g}{RT}\right)}{2p_g\chi\sigma\dot{\varepsilon}_{disl}}\right)^{\frac{1}{1+p_g}}. \quad (2)$$

Table 1. Parameter Values for the Steady State Grain-Size Evolution Model (Equation (2)) [*Behn et al.*, 2009]

G_0 (m^{Pg} s^{-1})	p_g	λ	γ	χ	c	E_g (J/mol)	V_g (m^3/mol)
4.5×10^{-4}	3	3	1	0.1	3	3.50×10^5	8×10^{-6}

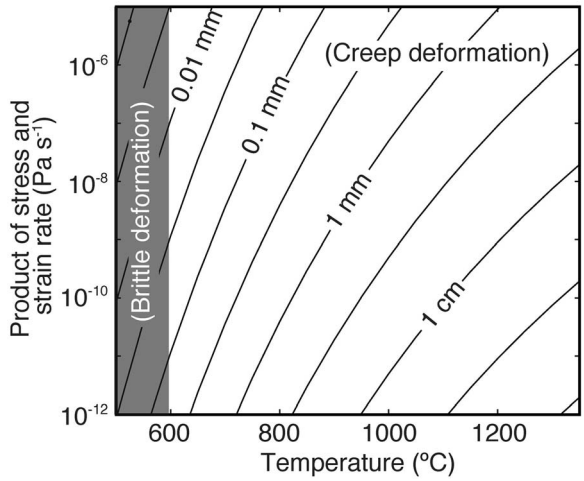

Figure 2. Steady state grain size calculated for the range of temperature and deformation conditions (expressed by the product of shear stress and dislocation-creep strain rate) that are expected for the creeping regions of the mantle wedge in the fore-arc and arc regions.

As grains travel through the mantle wedge, their size evolves toward steady state with the changing thermal and deformation conditions. For typical mantle wedge conditions, we find that the rate at which the grain size evolves toward steady state is much faster than the rate at which the thermal and deformation conditions change (see Appendix A). This implies that the grain size can be approximated based on its steady state value. The one exception is just above the slab, where grain growth kinetics are slightly slower than those in the rest of the creeping region (see Appendix A). In sections 3 and 4, we discuss how the slower grain growth kinetics may affect the grain-size distribution derived from our modeling results. For the range of temperature and deformation conditions expected for the fore-arc and subarc mantle wedge, the expected range of d_{ss} is ~10 μm to a few centimeters (Figure 2).

[9] Using the *A&E* GSE model, we solve for the grain size everywhere in the mantle wedge. However, the model does not account for the effect of brittle deformation and is applicable only in regions where creep deformation is the dominant deformation mechanism. We approximate the brittle-ductile transition by the 600°C isotherm and interpret our results only for the region with >600°C (hereafter referred to as the creeping region).

[10] Secondary phases, such as pyroxene and spinel, are present in naturally occurring mantle rock, and their presence limits grain boundary migration and thus "pin" the maximum extent of grain growth [*Olgaard and Evans*, 1986]. The pinning-limited grain size of the primary phase depends on the grain size of secondary phases and the spacing between them, which are in turn controlled by a process called Ostwald ripening [*Lifshitz and Slyozov*, 1961]. This process is limited by the solubility and diffusivity of secondary phase material in the matrix and results in the coarsening of secondary-phase particles and an increase in spacing between the particles. At mantle wedge conditions, secondary phases such as pyroxene are likely stable [*Behn and Kelemen*, 2006; *Hacker*, 2008]. Laboratory experiments on grain-size evolution of olivine in the presence of pyroxene indicate that the maximum extent of olivine grain growth is about a few centimeters because of the combined effects of Ostwald ripening and grain boundary pinning [*Evans et al.*, 2001, and references therein]. The *A&E* GSE model is based on experimental data on a single-phase (olivine) system and thus does not include the effect of grain boundary pinning. We will, however, test this effect on the grain-size distribution by prescribing an upper bound on the maximum extent of grain growth of a few centimeters in section 3.1.

[11] In addition to the effects of pinning, GSE models based on single-phase systems are likely to overestimate grain growth kinetics in the presence of secondary phases because the solubility and diffusivity of the secondary phase is slower than the diffusivity of material across grain boundaries of the primary phase [e.g., *Wang et al.*, 1996; *Ohuchi and Nakamura*, 2007]. Opposite effects are likely to be exerted by the presence of a fluid phase (water and/or melts), which allows faster grain boundary migration because of enhanced lattice or boundary diffusion kinetics [*Cooper and Kohlstedt*, 1986; *Karato*, 1989; *Hirth and Kohlstedt*, 1995a, 1995b].

2.2. Mantle Rheology Model

[12] We adopt a composite mantle rheology that accounts for both dislocation creep and diffusion creep and use parameters determined for wet olivine [*Hirth and Kohlstedt*, 2003; *Behn et al.*, 2009] (See Table 2 for parameter values). The general form of the flow law for diffusion creep and dislocation creep is

$$\dot{\varepsilon}_i = A_i d^{-p_i} \sigma^{n_i} C_{OH}^{r_i} \exp\left[-\frac{E_i + PV_i}{RT}\right] \tag{3}$$

where A is the preexponential factor; p is grain-size exponent, n is the stress exponent, C_{OH} represents water content, and r is the water exponent [*Karato and Wu*, 1993]. The subscript i denotes the deformation mechanism, either "disl" for dislocation creep or "diff" for diffusion creep. Dislocation creep is grain-size independent, and thus p_{disl} is zero. The flow law above is cast into a form suitable for 2-D and three-dimensional (3-D) modeling by defining the viscosity η_i for each deformation mechanism:

$$\eta_i = \left(A_i d^{-p_i} C_{OH}^{r_i} \exp\left[-\frac{E_i + PV_i}{RT}\right]\right)^{-\frac{1}{n}} \dot{\varepsilon}_i^{\left(\frac{1-n}{n}\right)}. \tag{4}$$

Diffusion and dislocation creeps operate in parallel, and the total strain rate ($\dot{\varepsilon}_{total}$) is the sum of the two strain rates:

$$\dot{\varepsilon}_{total} = \dot{\varepsilon}_{diff} + \dot{\varepsilon}_{disl}. \tag{5}$$

[13] The mechanism that operates at a faster rate represents the dominant deformation mechanism. In our model,

Table 2. Rheological Parameter Values for Wet Olivine (Equation (4)) [*Hirth and Kohlstedt*, 2003; *Behn et al.*, 2009]

Creep	A (Pa^{-n} s^{-1})	n	p	r	E (J/mol)	V (m^3/mol)	C_{OH} (H/10^6 Si)
Diffusion	0.333	1	3	1	3.35×10^5	4×10^{-6}	1000
Dislocation	3.0×10^{-20}	3.5	0	1.2	4.80×10^5	1.1×10^{-5}	1000

Table 3. Density and Thermal Properties Used in the Thermal Model

Material	Density (kg/m^3)	Thermal Conductivity (W/m K)	Radiogenic Heat Production ($\mu W/m^3$)
Upper crust	2750	2.5	1.3
Lower crust	2750	2.5	0.4
Mantle wedge	3300	3.1	0.02
Subducting slab	3300	3.1	0.02

we prescribe a maximum effective viscosity (η_{max}) to avoid unrealistically high shear stress, and the effective viscosity (η_{eff}) is described as

$$\eta_{eff} = \left(\frac{1}{\eta_{diff}} + \frac{1}{\eta_{disl}} + \frac{1}{\eta_{max}}\right)^{-1}. \quad (6)$$

We set the maximum effective viscosity to 10^{25} Pa s, which is large enough relative to the effective viscosity of the flowing part of the mantle that it has little effect on wedge flow.

[14] Recent studies indicate that dislocation glide, which follows an exponential flow law, may operate in the mantle wedge corner where shear stress is relatively high (>100 MPa) [*Katayama and Karato*, 2008]. However, as will be shown, our model predicts that the stress is largely <100 MPa in the creeping region, and thus the role of dislocation glide is likely to be negligible.

2.3. Thermal and Mantle-Flow Model

[15] To solve for grain size in the mantle wedge, we couple the GSE model described in section 2.1 with a 2-D steady state finite element thermal and mantle-flow model. The thermal and mantle-flow model consists of a subducting slab with kinematically prescribed motion, an overriding nondeforming 35 km thick crust, and a viscous mantle wedge with the composite mantle rheology described in section 2.2. The governing equations for heat transfer and conservation of mass and momentum for the thermal and mantle-flow model are as described by *Wada et al.* [2008], except that the effect of frictional heating along the plate interface is excluded in this paper since it is applicable only to the shallow part (<~30 km depth) of the interface and has little effect on the region of interest. At the depths of interest (<150 km depth), the PV terms in the grain-size evolution model (equation (2)) and the mantle rheology model (equation (3)) are small compared with E and are thus neglected in this paper. Material properties for all the subdomains are summarized in Table 3.

[16] Viscous coupling between the subducting slab and the overriding mantle drives wedge flow, which controls the thermal and deformation conditions in the mantle wedge. To satisfy geophysical observations, such as surface heat flow and seismic attenuation data and petrologically and geochemically constrained subarc mantle temperature, subduction zone thermal modeling studies have showed that the slab and the mantle are decoupled at relatively shallow depths, and the downdip change from decoupled to coupled interface occurs at a relatively uniform depth of 70–80 km [e.g., *Honda*, 1985; *Furukawa*, 1993; *Kincaid and Sacks*, 1997; *van Keken et al.*, 2002; *Currie et al.*, 2004; *Wada and Wang*, 2009] (Figure 1). To be consistent with these observations and previous thermal modeling studies, a maximum depth of decoupling (MDD) of ~75 km is assumed, unless otherwise stated.

[17] The degree of slab-mantle coupling is controlled by the strength contrast between the interface and the overriding mantle. Following *Wada et al.* [2008], we apply a thin layer with a uniform thickness (100 m) and a uniform viscosity (η') to the slab-mantle interface to represent the strength of the interface in our model (Figure 1). Although the interface strength does not vary with depth in the model, its strength contrast with the mantle decreases with depth because the mantle becomes weaker with increasing temperature. This leads to a rheologically controlled transition from a decoupled to a coupled interface, and this transition marks the MDD. In our models, we prescribe a value of η' such that the MDD is ~75 km. This approach simulates a range of stress conditions along the interface from full decoupling to full coupling without having to prescribe them and thus allows better inferences of the deformation conditions and the grain-size distribution in the mantle wedge than other approaches with a fixed-velocity or fixed-stress condition along the interface.

[18] The geotherm for the incoming oceanic plate of a given age is calculated by using the GDH1 plate cooling model [*Stein and Stein*, 1992]. This model assumes a 95 km thick lithosphere with a basal temperature of 1450°C. We assign this geotherm to the trench-side vertical boundary of the model and a constant temperature of 1450°C to the bottom boundary of the 95 km thick slab.

[19] The geotherm assigned to the shallow part (<~60 km depth) of the back-arc side vertical boundary is calculated by using a one-dimensional (1-D) steady state conductive heat equation to give the observed average back-arc surface heat flow of 80 mW/m^2 [*Currie and Hyndman*, 2006]. To the deeper part of the back-arc vertical boundary, we assign a geotherm calculated by assuming a back-arc mantle potential temperature (T_m) of 1350°C [e.g., *Herzberg et al.*, 2007; *Putirka*, 2008] and an adiabatic temperature gradient of 0.3°C/km, unless otherwise stated. A constant temperature of 0°C is assigned to the top boundary of the model.

[20] The heat and flow equations are solved simultaneously and iteratively. At each iteration, the steady state grain size used in the grain-size-dependent diffusion-creep portion of the flow equations (equation (3)) is calculated from equation (2) with stress and dislocation-creep strain rate taken from the previous iteration. The solution is considered to have converged when the residuals of temperature, velocity, and dynamic pressure (defined as the maximum difference between consecutive iterations normalized by the values in the respective fields) are reduced to 10^{-6}. The convergence of the solutions for the heat and flow equations naturally leads to the convergence of steady state grain size because of the mutual dependence of grain size, temperature, and mantle rheology on one another. The maximum difference in the grain size between the last and second-to-last iterations normalized by the value from the second-to-last iteration before convergence is typically of the order of $\sim 10^{-4}$.

[21] We use simple slab geometries with a constant dip to facilitate comparison between models with different subduction parameterization. The width of the model domain is set such that the distance between the horizontal position of the MDD and the back-arc side vertical boundary is 150 km

Table 4. Model Parameters

Slab Age (Ma)	Subduction Rate (cm/yr)	Slab Dip (°)	Back Arc T_m (°C)	MDD (km)	η' (Pa s)	Figure
10	4	30	1350	75	3.8×10^{18}	3
100	4	30	1350	75	5.0×10^{19}	5a, 5b
10	8	30	1350	75	4.0×10^{18}	5c, 5d
10	4	60	1350	75	4.9×10^{18}	5e, 5f
10	4	30	1250	75	4.9×10^{18}	6a, 6b
10	4	30	1450	75	2.7×10^{18}	6c, 6d
10	4	30	1350	65	1.8×10^{18}	7a, 7b
10	4	30	1350	90	5.8×10^{18}	7c, 7d

in all models. We note that some geophysical and geological observations indicate a complex 3-D mantle wedge flow [*Tamura et al.*, 2002; *Hoernle et al.*, 2008; *Wiens et al.*, 2008]. Various mechanisms for three-dimensional mantle flows have been proposed, including Rayleigh-Taylor-type instabilities from the subducting slab [e.g., *Zhu et al.*, 2009], foundering of the lower crust off the base of the overriding plate [e.g., *Behn et al.*, 2007], pressure gradients caused by variations in slab geometry along the margin [e.g., *Kneller and van Keken*, 2008], and the edge effects of the subducting slab [e.g., *Piromallo et al.*, 2006]. In this paper, however, we focus on the effect of slab-driven mantle wedge flow on grain-size evolution.

[22] We found that in all the models that we developed, the smallest grain size in the creeping region is of the order of 10–100 μm, which is comparable to that of the smallest grain sizes in mantle xenoliths (section 1). We also found that prescribing a minimum grain size of 10 μm or less does not affect the model result in the creeping region. Therefore, in all of our models except in the reference model, we prescribe a lower limit of 10 μm.

3. Modeling Results

[23] We developed a suite of models for different subduction parameterizations (Table 4). Below, we first present one of these models for the purpose of describing the key characteristics of the grain-size distribution and its relation to the thermal and deformation fields in the creeping region of the mantle wedge. This model has a slab age of 10 Ma, a subduction rate of 4 cm/yr, and a slab dip of 30°. Using this model as a reference model, we then describe how the grain-size distribution changes with subduction parameters and assumed values of the back arc T_m and the MDD (section 2.3).

3.1. Grain-Size Distribution Characteristics

[24] Significant changes in the temperature and deformation conditions occur over relatively short distances within the wedge (Figures 3a–3d), giving rise to a large spatial variation in grain size (Figure 3e). Temperature increases from 600°C at the most trenchward part of the creeping region to >1300°C in the subarc mantle (Figure 3a), resulting in the lowest rate of grain growth toward the trench. The product of shear stress and dislocation-creep strain rate (the driving force for dynamic recrystallization) varies by more than 7 orders of magnitude (10^{-13}–10^{-6} Pa s^{-1}) across the creeping region (Figures 3b–3d), reaching a maximum immediately above the MDD. The thermal and deformation fields together thus result in a general increase in grain size from the corner of the mantle wedge above the MDD toward the subarc mantle (Figure 3e).

[25] On the basis of the grain-size distribution, four subregions can be identified within the creeping region (subregions I, II, III, and IV in Figure 3e). Subregion I immediately above the MDD is characterized by a sharp arcward increase in grain size, from ~30 μm to 1 cm over a distance of ~12 km in the reference model (Figure 4a). This sharp increase is caused by a combination of the sudden increase in temperature from the shallower cold stagnant mantle to the deeper hot flowing mantle (Figure 3a) and the sharp decrease in shear stress from the MDD toward the hotter and weaker subarc mantle (Figure 3b). In subregion II at the base of the creeping region, the strong thermal contrast between the subducting slab and overriding mantle causes a sharp upward increase in temperature and grain size. In the downdip direction, however, grain size increases more gradually (Figure 4b) because the downdip changes in the thermal and deformation condition are more subdued. Moreover, we note that the downdip increase may even be more gradual if the grain size does not reach steady state because of the slower grain growth kinetics in this subregion compared with those of the other subregions (see Appendix A). Subregion III in the shallow, nearly stagnant part of the creeping region is also characterized by a gradual arcward increase in grain size that is due a to lateral change in the thermal and deformation conditions. Finally, subregion IV beneath the arc is characterized by largest grain sizes (>1 cm) because of the high-temperature and low-deformation conditions. The implications of these variations in grain size for fluid-melt transport and the seismic properties of the mantle wedge are discussed in section 4.

[26] Although our models predict that grains can grow to 20–30 cm in the hottest part of the subarc mantle, grain sizes that are greater than a few centimeters are rare in mantle xenoliths (section 1). As discussed above (section 2.1), the maximum extent of grain growth is limited by the presence of secondary phases via grain boundary pinning; however, this effect is not included in the *A&E* GSE model, which is based on a single-phase system. Thus, we interpret these large grain sizes in subregion IV as an indication that grain boundary pinning places an upper bound on olivine grain size in this subregion.

[27] To test whether secondary-phase pinning affects the distributions in the rest of the creeping region, we performed a series of calculations with an imposed upper limit on grain size ranging from d_{max} = 1 to 20 cm. We found that the maximum grain size is limited by d_{max} in subregion IV, where the model without pinning predicted larger grain sizes. However, in all models with a prescribed d_{max}, the grain-size distributions in the rest of the creeping region are almost identical to those predicted by the model without a prescribed d_{max} (Figure 3e). These results indicate that grain boundary pinning, which likely controls the maximum grain size in subregion IV, does not affect the grain growth in other subregions.

3.2. Effects of Subduction Parameters, T_m, and the MDD on Grain-Size Distribution

[28] We next examined the effect of subduction parameters (slab age, subduction rate, slab dip, and MDD) on the distribution of grain size in the mantle wedge. Compared with

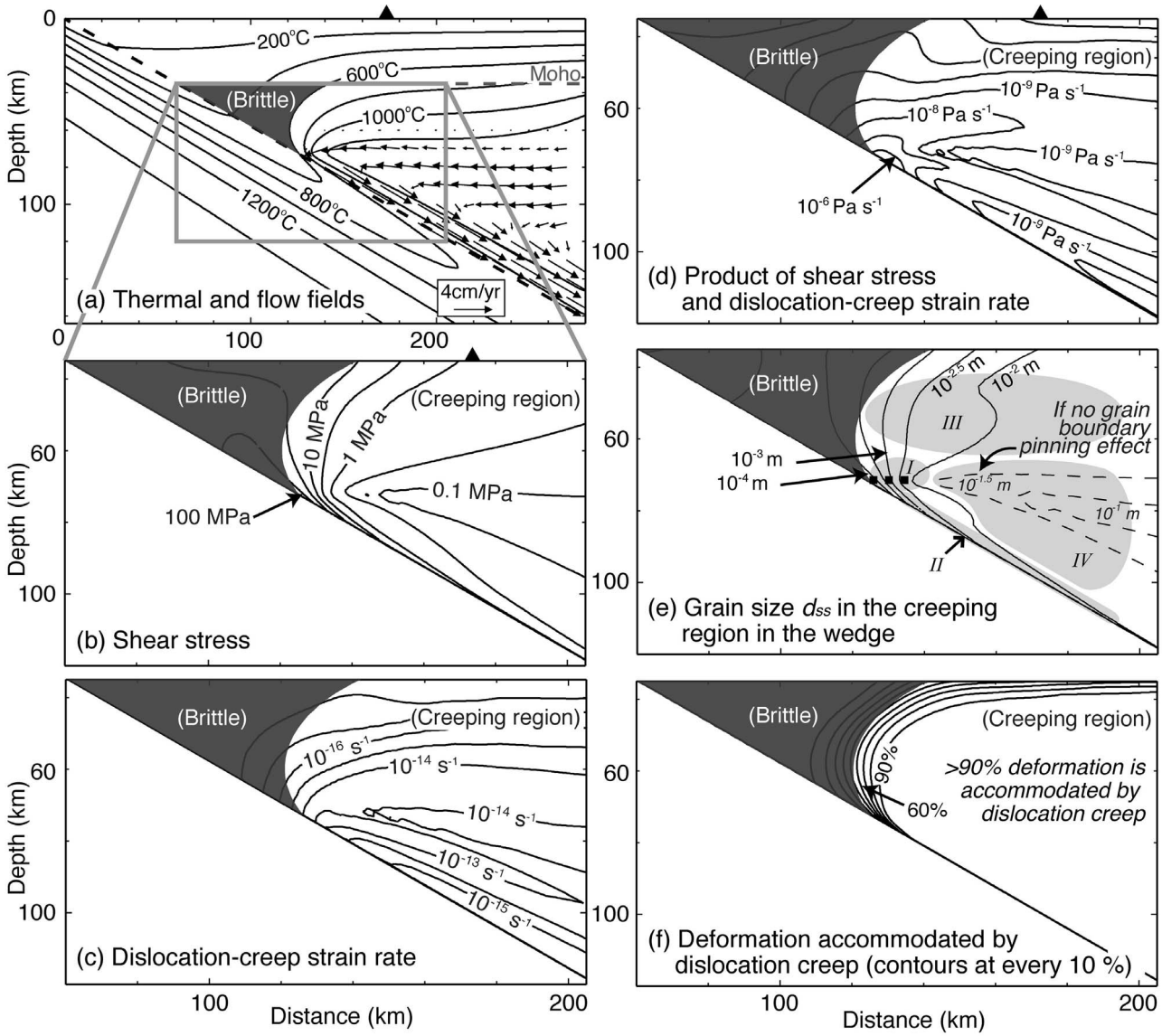

Figure 3. The reference model with a slab age of 10 Ma, slab dip of 30°, and subduction rate of 4 cm/yr ($\eta' = 3.8 \times 10^{18}$ Pa s). The model assumes a back arc T_m of 1350°C and an MDD of 75 km. (a) Thermal and flow fields, (b) shear stress, (c) dislocation-creep strain rate, (d) the product of shear stress and dislocation creep strain rate, (e) grain size, and (f) the percentage of deformation accommodated by dislocation creep. No upper limit on the grain size is placed in this model. Grain sizes >3 cm (dashed contours) are unlikely to occur in natural settings because of the effect of grain boundary pinning by secondary phases. The dark gray region in each part indicates where the temperature is <600°C. Light gray regions in 3e indicate subregions of different characteristics in the grain-size distribution discussed in the text. The thick dotted line in 3e indicates a profile line for Figure 4a. Other models exhibit a similar distribution of deformation by dislocation creep, as shown in 3f. Solid triangles at the top of the panels indicate the expected location of the volcanic arc, which typically occurs where the slab is about 100 km deep.

that of the reference model, the subduction of an older, colder slab (100 Ma) causes a cooler condition in the shallow stagnant wedge corner ("brittle" region) and at the base of the deeper part of the wedge (Figure 5a). By contrast, in the flowing portion of the wedge, temperatures are similar to those in the reference model because the thermal effect of the colder slab is overshadowed by the heating effect of the hot, flowing mantle. Thus, except in the shallowest part of the creeping region, the thermal and deformation conditions are very similar to those predicted by the reference model. The cooler condition in the "brittle" region makes a stronger thermal contrast with the flowing part of the mantle, resulting in a more rapid arcward temperature increase in subregion I. Because the mantle rheology is strongly temperature dependent, this temperature increase leads to an abrupt arcward decrease in shear stress. These thermal and deformation conditions result in a sharper arcward increase in grain size in subregion I (Figures 4a and 5a), as well as in

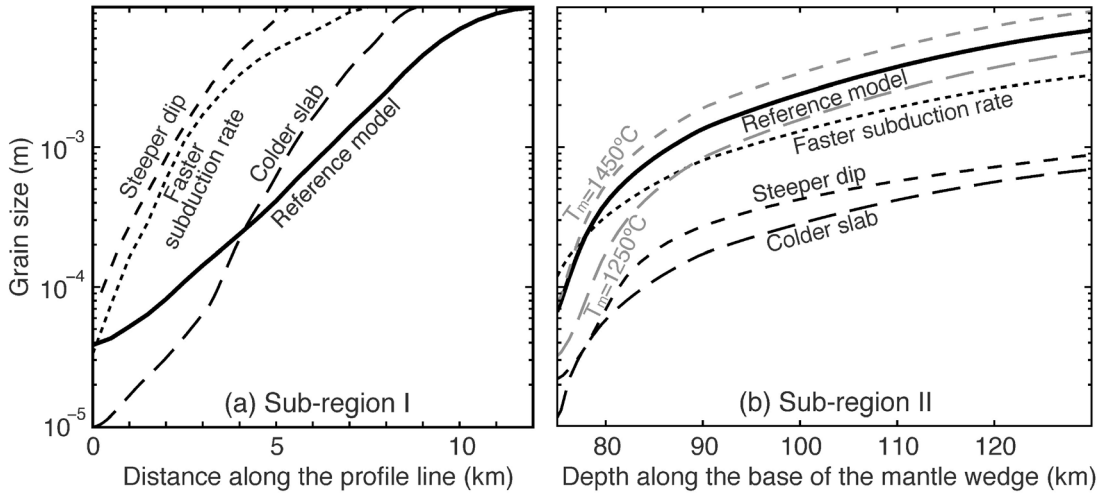

Figure 4. Grain size variation along (a) the profile line in subregion I (thick dotted line in respective figures for the grain-size distribution) and (b) the slab-wedge interface in subregion II (50 m above the slab surface) predicted by models shown in Figures 3, 5, 6, and 7.

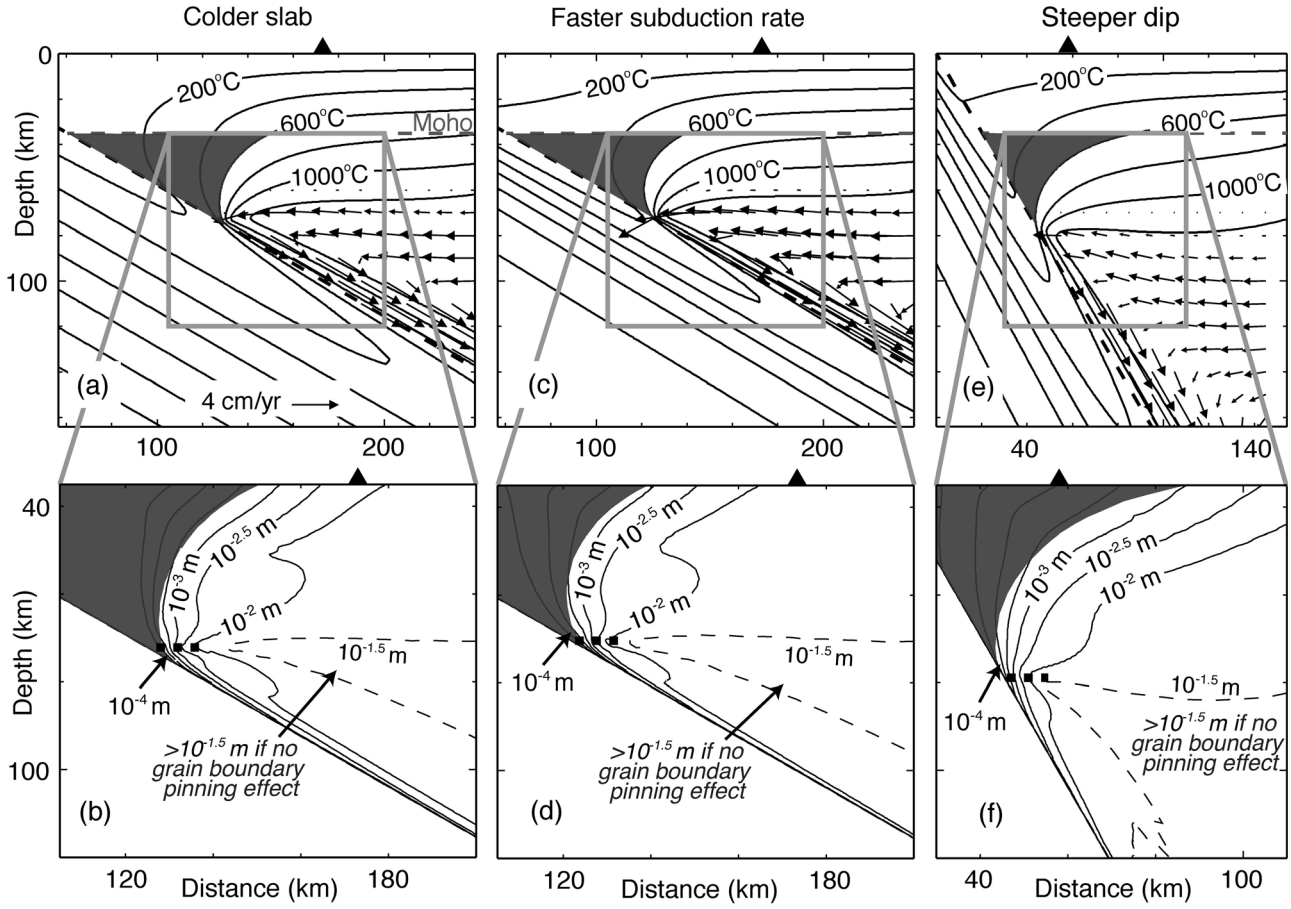

Figure 5. Thermal and flow fields (top) and grain-size distribution (bottom) predicted by models with (a, b) an older (100-Ma), colder slab ($\eta' = 5.0 \times 10^{19}$ Pa s), (c, d) a faster subduction rate of 8 cm/yr ($\eta' = 4.0 \times 10^{18}$ Pa s), and (e, f) a steeper slab dip of 60° ($\eta' = 4.9 \times 10^{18}$ Pa s). Thick dotted line in Figures 5b, 5d, and 5f indicates a profile line for Figure 4a.

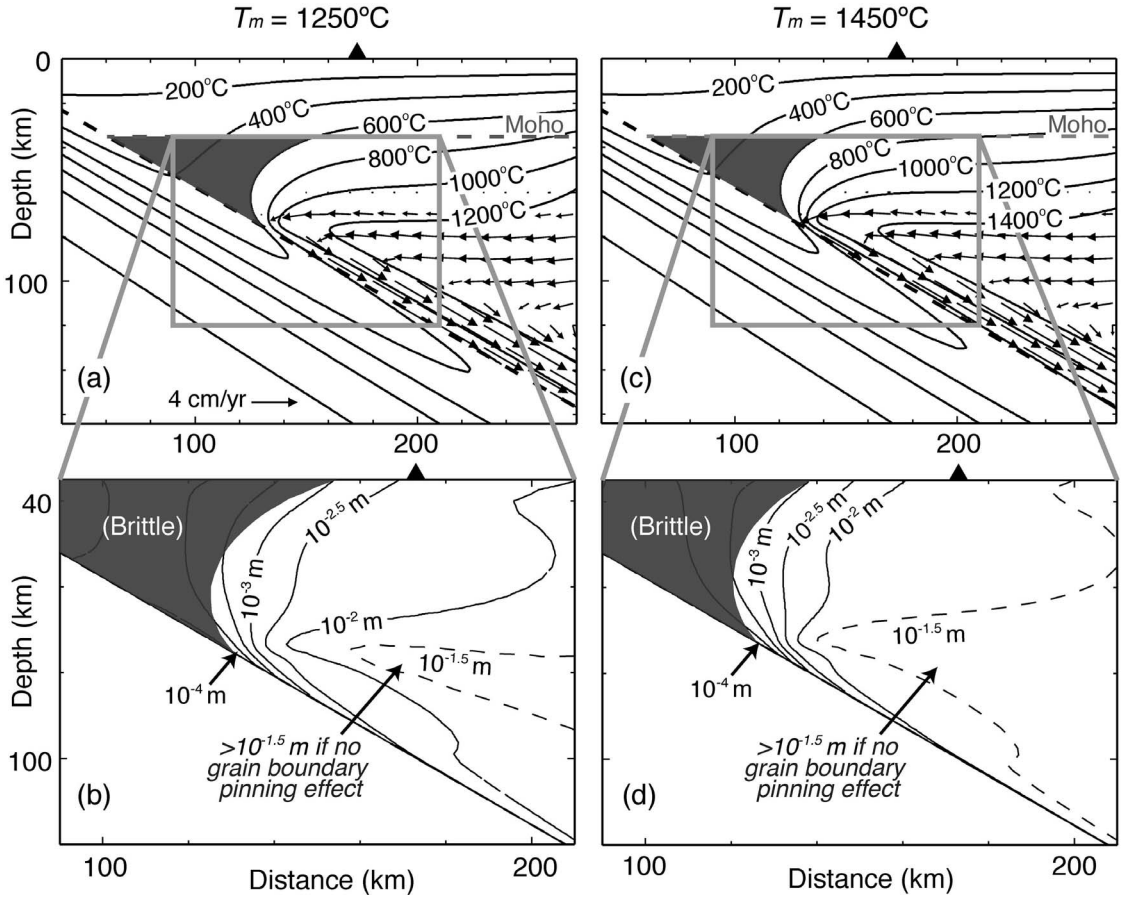

Figure 6. (top)Thermal and flow fields and (bottom) grain-size distribution predicted by models with (a, b) a colder back arc T_m of 1250°C ($\eta' = 4.9 \times 10^{18}$ Pa s) and (c, d) a hotter back arc T_m of 1450°C ($\eta' = 2.7 \times 10^{18}$ Pa s), relative to the reference model (Figure 3).

subregion III compared with the reference model. Moreover, in subregion II, the cooler condition along the interface results in systematically finer grain sizes (Figure 4b). In subregion IV, grain size is uniformly large as in the reference model owing to the dominance of grain growth associated with the hot flowing mantle in this subregion.

[29] Faster subduction rates advect the cold slab into the mantle more rapidly, leading to colder temperatures in the slab at a given depth compared with the reference model (Figure 5c). This leads to a cooler wedge base (subregion I) and systematically smaller grain size than in the reference model (Figures 4b and 5d). Faster subduction also drives a more vigorous mantle wedge flow, supplying more hot material to the fore arc. This leads to slightly higher temperature in the flowing part of the wedge, resulting in a larger region of uniformly large grain size in subregion IV (Figure 5d). The cooler slab and hotter subarc mantle lead to a sharper arcward increase in temperature and grain size in subregion I (Figure 4a). A steeper slab dip also results in deeper advection of the slab isotherms and thus causes slightly cooler conditions in subregions I and II (Figure 5e), compared with those of the reference model. This also results in a sharper arcward grain size increase in subregion I and systematically finer grain sizes in subregion II (Figures 5f and 4).

[30] The amount of heat advected into the wedge by mantle flow depends strongly on the thermal state of the back arc and deeper mantle. Recent petrological estimates for the T_m at midocean ridges are in the range of 1250°C–1450°C [e.g., *Herzberg et al.*, 2007; *Putirka*, 2008], and those for the T_m in back arcs are in the range of 1350°C–1500°C [*Kelley et al.*, 2006], indicating that there can be regional variations in the mantle wedge temperatures of up to 200°C that are due to variations in back arc T_m. To understand the effect of variations in T_m on mantle wedge temperature and grain size, we constructed models with T_m = 1250°C and 1450°C to compare with the reference model (Figure 6). The results show that a higher T_m causes systematically higher temperatures and larger grain sizes in subregion IV and a more rapid arcward increase in temperature and grain size in the other three subregions (Figure 4b).

[31] The above results indicate that while the details of the grain-size distribution vary with subduction parameters and T_m, the key characteristics of the grain-size distribution are relatively consistent across a wide range of subduction parameters. Specifically, all models predict a sharp arcward increase in grain size above the MDD (subregion I), a gradual downdip increase at the base of the wedge (subregion II), a gradual arcward increase in the shallow part of

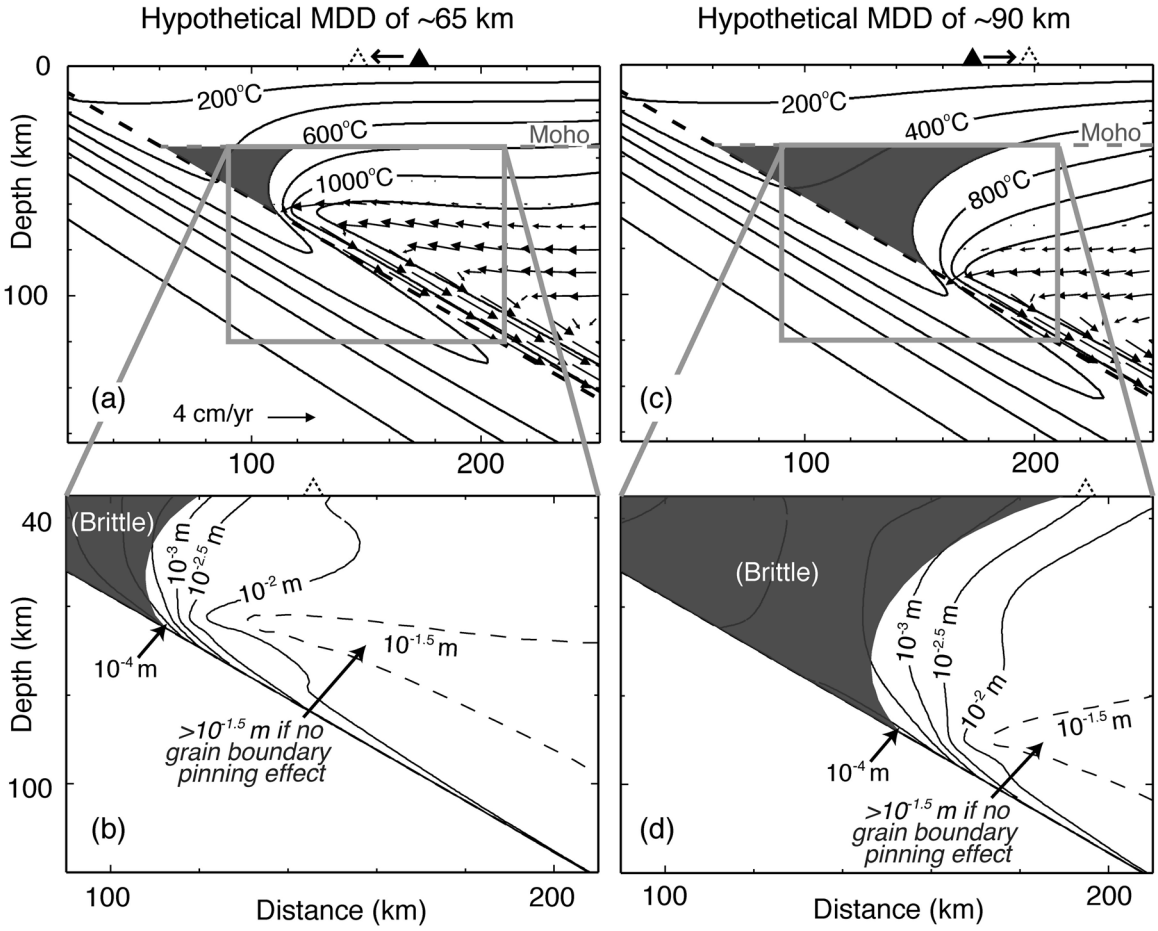

Figure 7. (top)Thermal and flow fields and (bottom) grain-size distribution predicted by models with (a, b) a shallower MDD of 65 km ($\eta' = 1.8 \times 10^{18}$ Pa s) and (c, d) a deeper MDD of 90 km ($\eta' = 5.8 \times 10^{18}$ Pa s), relative to the reference model (Figure 3). Arrow and dashed triangle at the top of 7a and 7c indicate the expected direction of shift in the location of arc as a result of the change in the wedge thermal structure that is due to the deviation of the MDD from its common 70–80 km depth.

the wedge (subregion III), and a uniformly large grain size beneath the arc with the maximum size controlled by grain boundary pinning (subregion IV). The consistency in the locations of the characteristic subregions results from the assumption of a common MDD, which gives rise to a relatively invariant flow and thermal fields in the creeping region. Deviations of the MDD from this common depth, which are due, for example, to a temporal change in regional tectonics or slab geometry, will lead to a systematic change in the thermal and flow fields in the wedge (Figures 7a and 7c). Because of the dependence of grain size on temperature and deformation, the absolute locations of the characteristic subregions shift systematically with the MDD, but without altering their key distribution characteristics (Figures 7b and 7d). Furthermore, the geometric relations between the locations of the MDD, the four subregions, and the arc are unaffected by the MDD.

3.3. Effect of Grain Size on Mantle Rheology, Flow, and Temperature

[32] To first order the spatial variations in grain size have little influence on the overall pattern of mantle wedge flow. This occurs because in the majority of the creeping region more than 90% of the deformation is accommodated by grain-size-independent dislocation creep in all models (e.g., Figure 3f). This implies that the application of a dislocation-creep rheology in kinematic subduction zone models, as commonly practiced [e.g., *van Keken et al.*, 2002; *Currie et al.*, 2004], provides a reasonable approximation of the flow and thermal fields.

[33] Grain size, however, has an important effect on the absolute strength of the overriding mantle, particularly at the base of the mantle wedge. We found that for the same interface strength and subduction parameterization, the MDD is shallower by ~10 km in the reference model than in a model with a dislocation-creep rheology (results not shown). The shallower MDD indicates that the mantle with the composite rheology is slightly weaker, resulting in a smaller strength contrast with the interface and a shallower extent of decoupling along the interface. The weaker mantle results from the relatively fine grain size at the base of the wedge, weakening the mantle via diffusion creep. Therefore, models that do not include the effect of the grain-size dependence of the mantle rheology are likely to overestimate the strength of the mantle at the base of the wedge, where grain size is relative small.

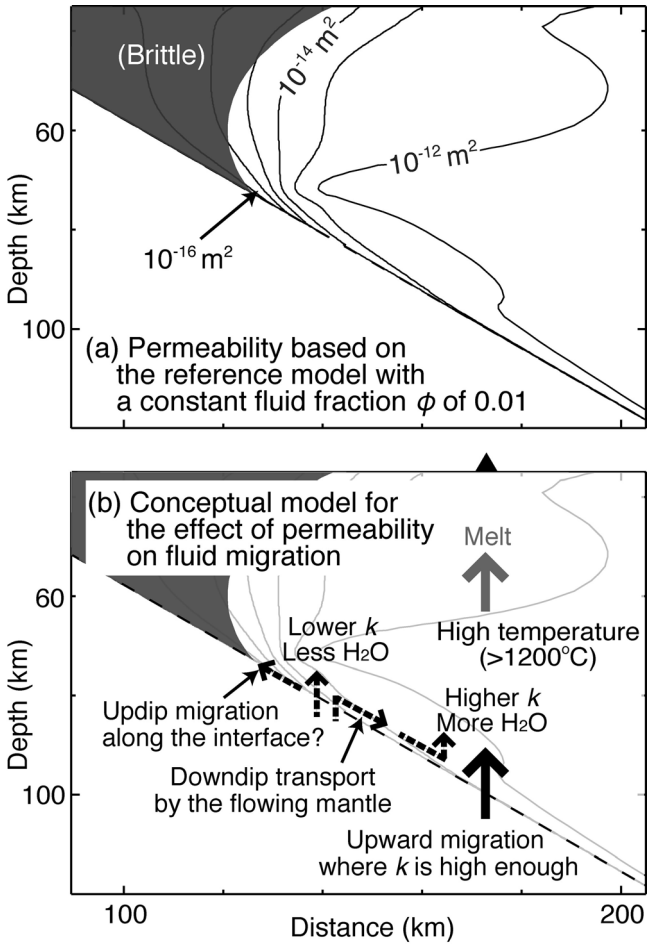

Figure 8. (a) Permeability in the mantle wedge calculated by using the reference model (Figure 3) and assuming ϕ = 0.01 and d_{max} = 3 cm. (b) Conceptual model for the effect of the permeability structure on the fluid migration and arc location. In 8b, thin gray curves are permeability contours from 8a, and the light gray region indicates a region with temperature >1200°C.

[34] The strength contrast between the mantle and the interface determines the degree and depth extent of slab-mantle coupling, as explained in section 2.3. It is not clear what causes the MDD to be relatively uniform. The thermal conditions along the slab-mantle interface are highly variable among different subduction zones, and thus the strongly temperature-dependent mantle strength is also expected to be highly variable. For example, a cooler interface leads to a stronger overriding mantle, which would lead to a deeper MDD (provided that the interface strength is relatively invariant). Therefore, the mantle strength is thought to be an unlikely factor that regulates the MDD. However, as presented in section 3.2, the cooler condition at the base of the wedge also leads to systematically finer grain sizes (Figure 4b) and thus a weaker mantle. In other words, the effect of grain-size evolution on the mantle strength competes with the thermal effect, reducing the variation in the mantle strength among different subduction zones. This effect of grain size on the mantle strength may partly be responsible for the apparent uniformity of the MDD. Finally, because the MDD may vary with changes in regional tectonics and/or slab geometry, grain-size evolution may be important in controlling slab evolution in dynamic subduction models that simulate changes in slab geometry and subduction initiation.

4. Implications of Grain-Size Variations on Mantle Wedge Dynamics

4.1. Grain-Scale Permeability in the Wedge and the Location of the Volcanic Arc

[35] At temperatures above the brittle-ductile transition, fluid migration occurs via porous flow through the interconnected pore space between grains. The common form of the empirical-derived relation between grain size and permeability k is

$$k = \frac{\phi^n d^2}{C} \tag{7}$$

where ϕ is the fluid fraction, C is a constant; and n ranges from 1 to 3 [e.g., *Wark and Watson*, 1998]. Using this relation and the predicted grain-size distribution, we calculated permeability in the creeping region (Figure 8a). In the calculation, we used C = 270 and n = 3, following *Wark et al.* [2003], and assumed ϕ = 0.01 and d_{max} = 3 cm. The grain-size distribution leads to an arcward increase in permeability by ~5 orders of magnitude in the creeping region, with the lowest permeability at the most updip part of the creeping region near the MDD (Figure 8a).

[36] Aqueous fluids play an important role in hydrous flux melting in the mantle wedge [e.g., *Grove et al.*, 2006], and thus their migration path is critical to the study of arc volcanism. To date, models of fluid migration in the mantle wedge have assumed a constant grain size [e.g., *Cagnioncle et al.*, 2007; *Hebert et al.*, 2009]; however, they are useful for understanding the importance of grain size on fluid migration. *Cagnioncle et al.* [2007] showed that if the mantle grain size is small (<~0.3 mm) the majority of fluids that enter the base of the wedge become trapped in the mantle because of its low permeability and are dragged downdip by the flowing mantle. However, if the grain size is relatively large (>~1 mm), the permeability is sufficiently high for the fluids to migrate upward through the wedge. From these results, we can interpret the importance of the grain-size and permeability variations predicted by our model to fluid transport in the mantle wedge.

[37] In most subduction zones, except where the slab is very young (<~15 Ma) and warm, the subducting crust starts to dehydrate as it approaches the MDD because of the heating effect of the hot flowing overriding mantle, resulting in a release of aqueous fluids over the depth range of 70–140 km [*Wada and Wang*, 2009]. However, we find that the permeability in the shallow part of the wedge base is relatively low (Figure 8a), owing to the fine grain sizes (Figure 4b). Fluids released from the slab at these depths may migrate updip along the plate interface if the permeability of the overlying interface material is sufficiently high (Figure 8b). Fluids that migrate into the wedge are likely to become trapped in the low-permeable mantle and dragged downdip. These trapped fluids are expected to migrate upward when they reach the more permeable deeper "wedge-base" mantle

Table 5. Parameter Values for the Shear Wave Attenuation Model (Equation (8)) [*Behn et al.*, 2009]

B (m^{Pq} s^{-1})	p_q	ω	α	E_q (J/mol)	V_q (m^3/mol)
1.6689×10^7	1	1	0.27	4.2×10^5	1.2×10^{-5}

(Figure 8b). As noted above, grain growth kinetics at the wedge base may not be fast enough to keep up with the changing thermal and deformation fields (see Appendix A). Thus, the narrow region of finer grains at the base may extend deeper than predicted, and trapped fluids may travel even farther downdip before they can migrate upward. By contrast, fluids released at deeper depths will migrate directly upward through the wedge, as there is no low-permeability barrier immediately above the interface. Thus, the predicted permeability distribution may lead to an optimal upward migration of aqueous fluids some distance downdip of the MDD and promote hydration melting and arc volcanism.

[38] The thermal state of the mantle wedge likely allows hydrous melting over a relatively wide region [*Grove et al.*, 2006], yet intriguingly, the arc tends to form at a relatively uniform location: above the point at which the slab reaches a depth of about 100–125 km [*England et al.*, 2004; *Syracuse and Abers*, 2006]. The grain-scale permeability variation at the wedge base may be an important factor that controls the focusing of melting beneath the arc by localizing the upward migration of fluids into the region of high temperature in the mantle wedge. Furthermore, because the grain-size distribution is generally consistent among different subduction zones, the optimal depth of permeability-controlled upward fluid migration is expected to be relatively invariant. This may help explain the paradox of why the subarc slab depth is relatively uniform [*England et al.*, 2004; *Syracuse and Abers*, 2006], 20–50 km deeper than the MDD.

[39] To fully quantify the effect of grain-size variations on fluid migration in the wedge, a self-consistent fluid migration model that incorporates spatial variations in both grain size and fluid fraction is needed. Such a model would help to understand the relative importance of different modes of volatile transport into the mantle wedge, i.e., the migration of slab-derived fluids via porous flow versus other proposed mechanisms, such as the migration of slab-derived melts [e.g., *Plank et al.*, 2009] and diapirism initiated by the buoyancy of subducted sediments [*Currie et al.*, 2007; *Behn et al.*, 2011] or hydrated mantle wedge material [e.g., *Hall and Kincaid*, 2001; *Gerya and Yuen*, 2003]. The effect of the H_2O entrapment on density variations and gravitational instabilities could also be tested through modeling fluid migration.

4.2. Grain-Size Effect on Seismic Attenuation in the Mantle Wedge

[40] Seismic attenuation, commonly described by Q^{-1}, is often used to infer a wedge thermal structure because of the strong temperature dependence of Q^{-1}. However, attenuation also depends on other factors, such as grain size, H_2O content, and the presence of melt. Laboratory experiments on melt-free olivine polycrystalline aggregates at upper mantle temperatures show a decrease in seismic wave speed and an increase in attenuation with decreasing grain size that is due to enhanced grain boundary sliding [*Jackson et al.*, 2002]. To calculate the effect of grain-size variation on Q^{-1}, we use an experimentally derived model for shear wave attenuation,

$$Q_s^{-1}(\omega, T, P, C_{OH}, d) = \left(B d^{-p_q} \omega^{-1} \exp\left(-\frac{(E_q + PV_q)}{RT} \right) \right)^{\alpha}, \tag{8}$$

where B is a preexponential factor calculated for C_{OH} of 1000 H/10^6 Si, p_q is the grain-size exponent, ω is frequency, and α is nondimensional frequency dependence [*Behn et al.*, 2009, and references therein] (parameter values are given in Table 5). The model does not include the effect of melt on attenuation. We use ω = 1 Hz, which is the frequency that has been used in the inversion of measurements for the shear wave attenuations in Costa Rica and Nicaragua [*Rychert et al.*, 2008] and Alaska [*Stachnik et al.*, 2004]. This model provides a good fit to the laboratory-derived attenuation data of *Tan et al.* [2001] and *Jackson et al.* [2002] and is comparable to the fit of the model of *Faul and Jackson* [2005]. Comparison of the model described by equation (8) to a more recent attenuation model of *Jackson and Faul* [2010] derived from newly obtained attenuation data indicates that the attenuation predicted here may be slightly higher (up to half an order of magnitude at high temperatures and a large grain size when calculated for a "dry" condition of C_{OH} = 50 H/10^6 Si), but the relative variation in attenuation with grain size and temperature remains robust.

[41] Seismic attenuation calculated from equation (8) and the predicted temperature and grain-size distribution increases from the most trenchward part to the hottest part of the subarc mantle (Figure 9a). If a constant grain size of 1 cm is assumed, the subarc mantle is slightly more attenuating than for the variable grain-size distribution (Figure 9b), but the difference is within the range of observational uncertainties or regional variability [e.g., *Stachnik et al.*, 2004; *Rychert et al.*, 2008]. By contrast, if a constant grain size of 1 mm is assumed, the wedge becomes significantly more attenuating (Figure 9c). These results show that an assumption of a constant grain size of 1 cm can provide a first-order approximation when interpreting the observed subarc mantle attenuation; however, accounting for grain-size variations may be important for detailed studies of seismic attenuation.

[42] The shear wave attenuation structure of the mantle wedge has been reported for Costa Rica and Nicaragua [*Rychert et al.*, 2008] and central Alaska [*Stachnik et al.*, 2004]. The value for 1000/Q increases from <5 in the coldest part to 7–20 in the hottest part of the subarc mantle in the three subduction zones. The predicted attenuation structure (Figure 9a) is consistent with the trend and magnitude of the observed attenuation, indicating that the first-order characteristics of the attenuation structure can be explained by its dependence on temperature, grain size, and water content. Seismic attenuation structures reported for other subduction zones, such as Hikurangi [*Eberhart-Phillips et al.*, 2008], the central Andes [*Schurr et al.*, 2003], and northeast Japan [*Tsumura et al.*, 2000], cannot be directly compared with our modeling results because of differences in the seismic phase and parameterization used to calculate the attenuation, but they all show the same trend of increasing attenuation toward the subarc mantle.

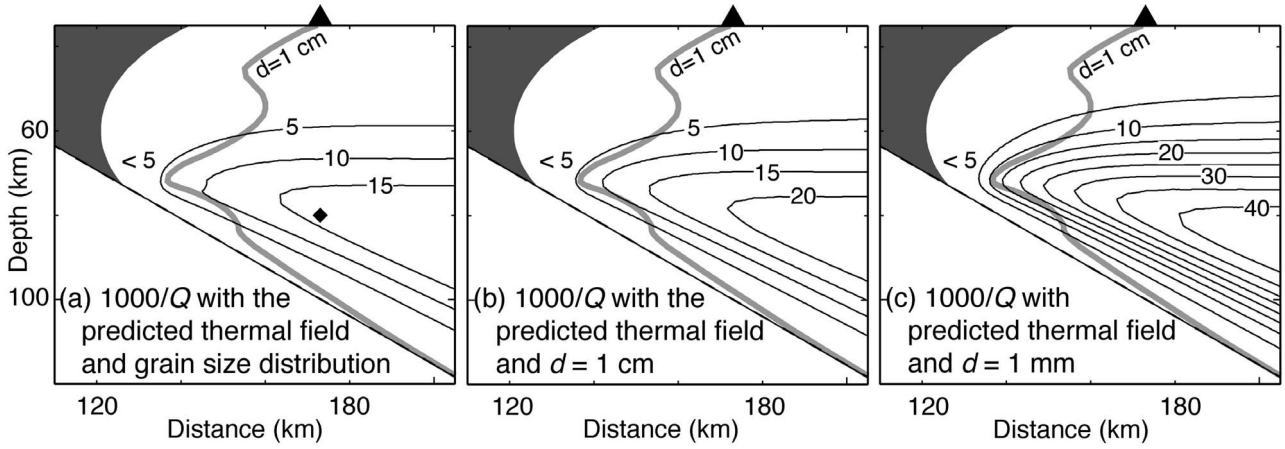

Figure 9. 1000/Q calculated from the reference model (). All three cases are calculated by using the predicted thermal structure, but based on (a) the predicted grain-size distribution with d_{max} = 3 cm, (b) a uniform grain size of 1 cm, and (c) a uniform grain size of 1 mm. The solid diamond in 9a indicates the data sampling point for Figure 10.

[43] The observed high subarc attenuation is often partially attributed to the presence of melt. Experimental observations suggest that the presence of melt facilitates grain boundary sliding, increasing seismic attenuation [*Faul et al.*, 2004]. Moreover, attenuation may be enhanced by relaxation via bulk melt flow [e.g., *Gribb et al.*, 1994]; however, this effect has yet to be quantified through experiments. On the other hand, experimental observations and theoretical treatments indicate that anelastic relaxation within individual melt pockets or via flow within connected pockets occurs at higher frequencies than the seismic band, resulting in no seismic attenuation [*Mavko*, 1980; *Faul et al.*, 2004].

[44] To assess whether attenuating effects of melt is required to explain the subarc attenuation observations in Nicaragua, Costa Rica, and Alaska, we calculated subarc attenuation for an expected range of back arc T_m, C_{OH}, and d_{max} (equation (8)). For C_{OH} = ~1000 H/10^6 Si, the results show that the attenuation predicted for the expected range of d_{max} (1–3 cm) can satisfy the observed range in Nicaragua (Figure 10) as long as T_m is <~1400°C. The effect of melt can be added to the predicted values without exceeding the observed attenuation range: however, the magnitude of the effect is likely to be relatively small, particularly if T_m is ~1350°C. The observed attenuation in Costa Rica can be satisfied if T_m is <~1325°C, and there is even a smaller portion of the observed attenuation that requires additional effects of melt than in Nicaragua (Figure 10). In the wedge, the mantle may at or above saturation (C_{OH} > ~ 5000 H/10^6 Si [*Hirschmann et al.*, 2005]). The addition of water beyond its solubility in olivine further increases attenuation [*Karato*, 2003]. Therefore, in both Nicaragua and Costa Rica, it appears that the high subarc attenuation does not necessarily require a significant contribution by the presence of melt. Given that melt is almost certainly present in the mantle in both of these settings, a possible interpretation of our results is that melt is efficiently focused into melt channels and thus has a relatively small influence on the bulk seismic properties of the mantle wedge. Furthermore, depending on the partitioning of water into the melt phase, melting can even reduce attenuation [*Karato and Jung*, 1998]. Finally, to explain the observed attenuation in central Alaska requires T_m < 1250°C with little contribution of the melt effect (Figure 10). This inference is in good agreement with the

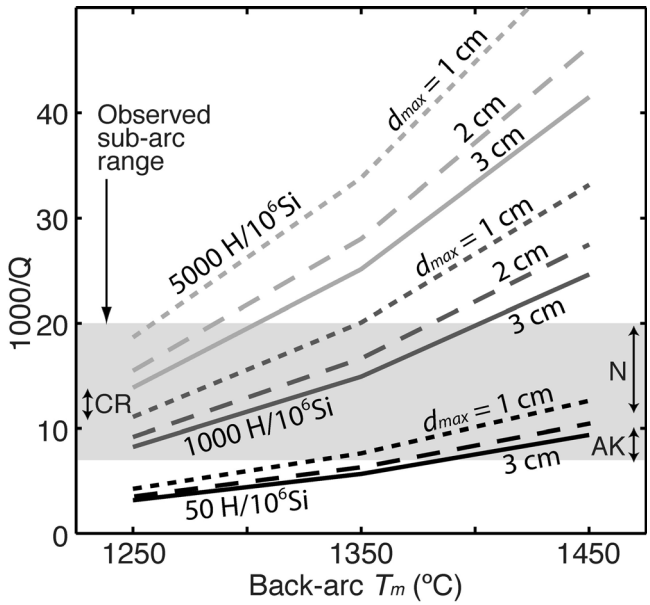

Figure 10. 1000/Q in the subarc mantle (the location is indicated by a solid diamond in Figure 9a) calculated by using a suite of modeling results for variable T_m, C_{OH}, and d_{max} and assuming ω = 1 Hz. The subduction parameterization of the reference model (Figure 3) is used in all models. Black, dark gray, and light gray curves indicate values for C_{OH} = 50, 1000, and 5000 H/10^6 Si, respectively. Dotted, dashed, and solid curves indicate values d_{max} = 1 cm, 2 cm, and 3 cm, respectively. The light gray region indicates the typical range of 1000/Q observed beneath the arc: Double-headed arrows with labels CR, N, and AK indicate the observed subarc values in Costa Rica, Nicaragua, and central Alaska, respectively [*Rychert et al.*, 2008; *Stachnik et al.*, 2004].

interpretation of the observed attenuation in central Alaska by *Stachnik et al.* [2004], i.e., that the subarc mantle is colder compared with that of other subduction zones, consistent with the absence of arc volcanism. Further observations on T_m and C_{OH} beneath the arc and experimental data on d_{max} at subarc mantle conditions will help isolate their effects on attenuation and in turn help us to understand the magnitude of the melt effect.

5. Conclusions

[45] In this paper, we calculated the steady state grain-size distribution in the creeping part of the mantle wedge, using a thermal and mantle-flow model coupled with the grain-size evolution model. The results showed that in all subduction settings, a fine grain size of 10–100 μm is found in the most trenchward portion of the creeping region, near the maximum depth of slab-mantle decoupling (MDD), and grain size increases rapidly arcward to a few centimeters over a short distance of ~10 km. At the base of the wedge, grain size increases more gradually downdip away from the MDD, reaching ~1 mm at 85–140 km depths. In the nearly stagnant top part of the creeping region, grain size increases gradually arcward. Within the hottest part of the creeping region, grain boundary pinning is likely to limit the maximum grain growth, leading to a uniform size of a few centimeters. Our results show that all subduction settings share these grain-size distribution characteristics and that the geometric relations between the characteristic subregions and the MDD are also consistent across a wide range of subduction settings.

[46] Grain size varies by more than 2 orders of magnitude within the creeping region, but its effect on the large-scale pattern of mantle wedge flow is small because grain-size-independent dislocation creep is the dominant deformation mechanism in the flowing part of the wedge. On the other hand, the decrease in grain size at the base of the wedge immediately above the slab results in a greater contribution of diffusion creep, weakening the mantle in this region. This weakening effect competes with the strengthening effect of the cool condition at the wedge base and moderates the variability in the mantle strength among different subduction settings, possibly controlling the strength contrast between the plate interface and wedge base. This rheological effect of grain size may partly be responsible for a common MDD of 70–80 km.

[47] The large variations in grain size throughout the wedge result in an arcward increase in grain-scale permeability by ~5 orders of magnitude. Fluids that migrate from the subducting slab into the shallow fore-arc part of the creeping region may become trapped in the fine-grained, low-permeable mantle immediately above the slab and dragged downdip. By contrast, the larger grains size above the slab at greater depths will promote a more efficient upward migration of fluids. Thus, the grain-size variations may help localize fluid migration and hydration melting over a relatively narrow region and regulate the location of the volcanic arc. The seismic attenuation structure derived from the predicted grain-size and temperature variations captures the first-order characteristics of observed attenuation structures: The value of $1000/Q$ increases from <5 in the most trenchward part of the creeping region to 10–20 beneath the arc. The high subarc attenuation does not appear to require a significant contribution by the presence of melt.

Appendix A: Evolution Toward a Steady State Grain Size

[48] Grain size in the mantle wedge can reach steady state with the thermal and deformation conditions if the change in grain size occurs faster than the change in these conditions as the grain travels through the wedge. We approximate this condition by

$$t_{\Delta d} < t_{\Delta x}, \tag{A1}$$

where $t_{\Delta d}$ and $t_{\Delta x}$ are the grain-size evolution time and travel time, respectively, of a grain that undergoes a change in grain size Δd as it travels over a small distance Δx along the mantle flow streamline. Here, we introduce a dimensionless time lag parameter, motivated by the use of a similar parameter in evaluating the efficiency of LPO development [e.g., *Kaminski and Ribe*, 2002],

$$\Pi = \frac{t_{\Delta d}}{t_{\Delta x}} \tag{A2}$$

such that, if $\Pi < 1$, grain size reaches steady state with its environment.

[49] For the models presented in this study, we calculate Π in the creeping region using the following approach. The models provide the steady state grain size (d_{ss1}), thermal and deformation conditions (T_1, σ_1, $\dot{\varepsilon}_{disl1}$), and flow velocity ($\vec{u}_1$) at a given point p_1 (Figure A1a). Using $\vec{u}_1$, we backtrack the position of a grain from p_1 to p_0 for a short distance Δx and obtain the steady state grain size (d_{ss0}) at p_0. The time it takes for d_{ss0} to grow or shrink to d_{ss1} at the thermal and deformation conditions at p_1 is $t_{\Delta d}$ and is calculated by integrating equation (1) (Figure A1b). Specifically, we assume a constant $t_{\Delta x}$ and calculate Δx from $\vec{u}_1\, t_{\Delta x}$. The smaller $t_{\Delta x}$ is, the smaller Δx will be and the more accurate the travel time estimate becomes. Given the model resolution, however, we cannot reliably resolve the grain-size variation below the 10 m scale in some portion of the creeping region, and therefore we choose $t_{\Delta x}$ such that Δx is <~100 m in the creeping region. For example, for a subduction rate of 4 cm/year in the case of the reference model, we use $t_{\Delta x} = 2500$ yr, and the largest Δx value is ~100 m, which occurs at the wedge base where the flow velocity is nearly compatible with the subduction rate. The relatively small values of Δx allow reasonable approximations for $t_{\Delta d}$. The small velocities in the nearly stagnant top part of the creeping region result in very small Δx, making it difficult to reliably resolve the difference in grain size over Δx. We exclude the top part the creeping region where Δx is <1 m from the Π calculation as this lies below the reasonable resolution of our model.

[50] The distribution of Π calculated for the reference model (Figure 3) is shown in Figure A2. Models with other choices of subduction parameters show a similar Π distribution. In the Π calculation, d_{max} of 3 cm is assumed (section 3.1). In the hottest part of the subregion IV, Π approaches zero because the grain size in that part of the subregion is fixed at d_{max}, resulting in $t_{\Delta d} = 0$ (Figures 3e and A2). In a narrow region where the flow direction

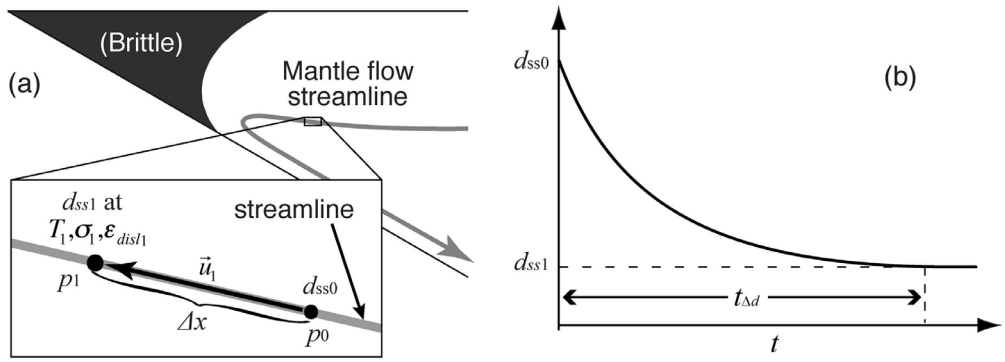

Figure A1. Schematic diagram illustrating (a) the variables and (b) the grain-size evolution time curve used to calculate the grain-size evolution time ($t_{\Delta d}$) and travel time ($t_{\Delta x} = \Delta x/\vec{u}_1$). The time curve is obtained from equation (1) with an initial condition of $d = d_{ss0}$ for each grid point.

changes rapidly over a short distance, the position of p_0 calculated from $\vec{u}_1$ deviates too far from the flow streamline to reliably determine Π (Figure A2). However, given that Π immediately outside of this region is $\ll 1$ and that the thermal and deformation conditions do not vary significantly across the boundary of the region, Π values in this region are likely to be <1. In the rest of the creeping region, Π is <1, indicating that the steady state assumption is reasonable (Figure A2). The one exception to this is at the base of the wedge in portions of subregion II, where Π approaches 1–10. In subregion II, grain size increases as it moves downdip. The relatively high Π indicates that there may not be sufficient time for the grain size to reach equilibrium with the thermal and deformation conditions, and thus the actual grain size may be smaller than the predicted steady state value. Therefore, the steady state GSE model provides a reasonable approximation in most part of the creeping region except at the wedge base, where it can overestimate grain size.

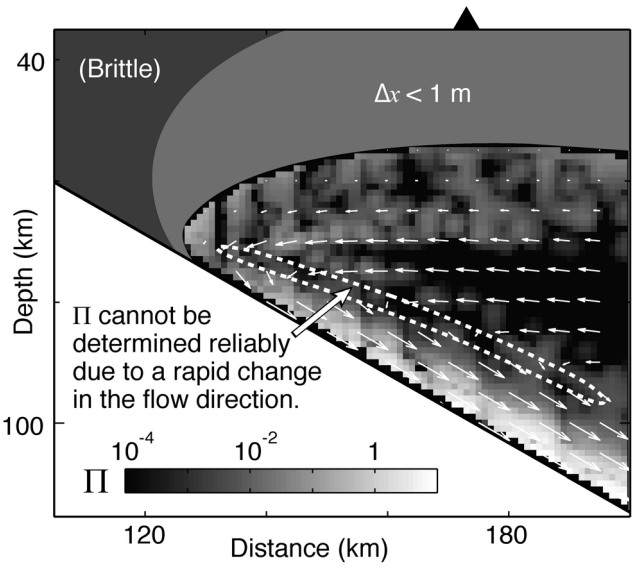

Figure A2. The grain-size evolution time lag parameter Π in the creeping region calculated at 1 km grid spacing for the reference model (Figure 3). White arrows indicate mantle-flow velocities. The top part of the creeping region where Δx is <1 m is excluded from the calculation because Δx is too small to reliably interpolate the difference in grain sizes over Δx. The white dashed curve indicates a region with rapid change in the mantle-flow direction. In the calculation of Π, $d_{max} = 3$ cm is assumed.

[51] **Acknowledgments.** Funding for this research was provided by the National Science Foundation through a MARGINS Postdoctoral Fellowship (NSF OCE-0840800) and NSF grant EAR-0854673. We thank Greg Hirth for fruitful discussions and Alison Shaw for useful comments on an earlier draft of this manuscript. We are grateful to two anonymous reviewers for helpful comments.

References

Aaronson, H. I. (1993), Atomic mechanisms of diffusional nucleation and growth and comparisons with their conterparts in shear transformations, *Metall. Trans. A*, *24*, 241–276, doi:10.1007/BF02657313.

Austin, N. J., and B. Evans (2007), Paleowattmeters: A scaling relation for dynamically recrystallized grain size, *Geology*, *35*, 343–346, doi:10.1130/G23244A.1.

Avé Lallemant, H. G., J.-C. C. Mercier, N. L. Carter, and J. V. Ross (1980), Rheology of the upper mantle: Inferences from peridotite xenoliths, *Tectonophysics*, *70*(1–2), 85–113, doi:10.1016/0040-1951(80)90022-0.

Behn, M. D., and P. B. Kelemen (2006), Stability of arc lower crust: Insights from the Talkeetna arc section, south central Alaska, and the seismic structure of modern arcs, *J. Geophys. Res.*, *111*, B11207, doi:10.1029/2006JB004327.

Behn, M. D., G. Hirth, and P. B. Kelemen (2007), Trench-parallel anisotropy produced by foundering of arc lower crust, *Science*, *317*, 108–111, doi:10.1126/science.1141269.

Behn, M. D., G. Hirth, and J. R. Elsenbeck II (2009), Implications of grain size evolution on the seismic structure of the oceanic upper mantle, *Earth Planet. Sci. Lett.*, *282*, 178–189, doi:10.1016/j.epsl.2009.03.014.

Behn, M. D., P. B. Kelemen, G. Hirth, B. R. Hacker, and H.-J. Massonne (2011), Diapirs as the source of the sediment signature in arc lavas, *Nat. Geosci.*, *4*, 641–646.

Bercovici, D., and Y. Ricard (2005), Tectonic plate generation and two-phase damage: Void growth versus grain size reduction, *J. Geophys. Res.*, *110*, B03401, doi:10.1029/2004JB003181.

Blatter, D. L., and I. S. E. Carmichael (1998), Hornblende peridotite xenoliths from central Mexico reveal the highly oxidized nature of subarc upper mantle, *Geology*, *26*, 1035–1038, doi:10.1130/0091-7613(1998)026<1035:HPXFCM>2.3.CO;2.

Cagnioncle, A.-M., E. M. Parmentier, and L. T. Elkins-Tanton (2007), Effect of solid flow above a subducting slab on water distribution and melting at convergent plate boundaries, *J. Geophys. Res.*, *112*, B09402, doi:10.1029/2007JB004934.

Cooper, R. F., and D. L. Kohlstedt (1986), Rheology and structure of olivine-basalt partial melts, *J. Geophys. Res.*, *91*, 9315–9323, doi:10.1029/JB091iB09p09315.

Currie, C. A., and R. D. Hyndman (2006), The thermal structure of subduction zone back arcs, *J. Geophys. Res.*, *111*, B08404, doi:10.1029/2005JB004024.

Currie, C. A., K. Wang, R. D. Hyndman, and J. He (2004), The thermal effects of steady-state slab-driven mantle flow above a subducting plate: The Cascadia subduction zone and back arc, *Earth Planet. Sci. Lett.*, *223*, 35–48, doi:10.1016/j.epsl.2004.04.020.

Currie, C. A., C. Beaumont, and R. S. Huismans (2007), The fate of subducted sediments: A case for backarc intrusion and underplating, *Geology*, *35*, 1111–1114, doi:10.1130/G24098A.1.

De Bresser, J. D., C. Peach, J. Reijs, and C. Spiers (1998), On dynamic recrystallization during solid state flow: Effects of stress and temperature, *Geophys. Res. Lett.*, *25*, 3457–3460, doi:10.1029/98GL02690.

De Bresser, J. D., J. ter Heege, and C. Spiers (2001), Grain size reduction by dynamic recrystallization: Can it result in major rheological weakening?, *Int. J. Earth Sci.*, *90*, 28–45, doi:10.1007/s005310000149.

Eberhart-Phillips, D., M. Reyners, M. Chadwick, and G. Stuart (2008), Three-dimensional attenuation structure of the Hikurangi subduction zone in the central North Island, New Zealand, *Geophys. J. Int.*, *174*, 418–434, doi:10.1111/j.1365-246X.2008.03816.x.

England, P., R. Engdahl, and W. Thatcher (2004), Systematic variation in the depths of slabs beneath arc volcanoes, *Geophys. J. Int.*, *156*, 377–408, doi:10.1111/j.1365-246X.2003.02132.x.

Evans, B., J. Renner, and G. Hirth (2001), A few remarks on the kinetics of static grain growth in rocks, *Int. J. Earth Sci.*, *90*, 88–103, doi:10.1007/s005310000150.

Faul, U. H., and I. Jackson (2005), The seismological signature of temperature and grain size variations in the upper mantle, *Earth Planet. Sci. Lett.*, *234*, 119–134, doi:10.1016/j.epsl.2005.02.008.

Faul, U. H., J. D. Fitz Gerald, and I. Jackson (2004), Shear wave attenuation and dispersion in melt-bearing olivine polycrystals: 2. Microstructural interpretation and seismological implications, *J. Geophys. Res.*, *109*, B06202, doi:10.1029/2003JB002407.

Furukawa, Y. (1993), Depth of the decoupling plate interface and thermal structure under arcs, *J. Geophys. Res.*, *98*, 20,005–20,013, doi:10.1029/93JB02020.

Gerya, T. V., and D. A. Yuen (2003), Rayleigh-Taylor instabilities from hydration and melting propel 'cold plumes' at subduction zones, *Earth Planet. Sci. Lett.*, *212*, 47–62, doi:10.1016/S0012-821X(03)00265-6.

Gribb, T. T., S. Zhang, and R. F. Cooper (1994), Melt migration and related attenuation in equilibrated partial melts, in *Magmatic Systems*, edited by M. P. Ryan, pp. 19–36, Academic, San Diego, Calif., doi:10.1016/S0074-6142(09)60090-5.

Grove, T. L., N. Chatterjee, S. W. Parman, and E. Medard (2006), The influence of H_2O on mantle wedge melting, *Earth Planet. Sci. Lett.*, *249*, 74–89, doi:10.1016/j.epsl.2006.06.043.

Hacker, B. R. (2008), H_2O subduction beyond arcs, *Geochem. Geophys. Geosyst.*, *9*, Q03001, doi:10.1029/2007GC001707.

Hall, P. S., and C. Kincaid (2001), Diapiric flow at subduction zones: A recipe for rapid transport, *Science*, *292*, 2472–2475, doi:10.1126/science.1060488.

Hall, C. E., and E. M. Parmentier (2003), Influence of grain size evolution on convective instability, *Geochem. Geophys. Geosyst.*, *4*(3), 1029, doi:10.1029/2002GC000308.

Hebert, L. B., P. Antoshechkina, P. Asimow, and M. Gurnis (2009), Emergence of a low-viscosity channel in subduction zones through the coupling of mantle flow and thermodynamics, *Earth Planet. Sci. Lett.*, *278*, 243–256, doi:10.1016/j.epsl.2008.12.013.

Herzberg, C., P. D. Asimow, N. Arndt, Y. Niu, C. M. Lesher, J. G. Fitton, M. J. Cheadle, and A. D. Saunders (2007), Temperatures in ambient mantle and plumes: Constraints from basalts, picrites, and komatiites, *Geochem. Geophys. Geosyst.*, *8*, Q02006, doi:10.1029/2006GC001390.

Hirschmann, M. M., C. Aubaud, and A. C. Withers (2005), Storage capacity of H_2O in nominally anhydrous minerals in the upper mantle, *Earth Planet. Sci. Lett.*, *236*, 167–181, doi:10.1016/j.epsl.2005.04.022.

Hirth, G., and D. Kohlstedt (1995a), Experimental constraints on the dynamics of partially molten upper mantle: Deformation in the diffusion creep regime, *J. Geophys. Res.*, *100*, 1981–2001, doi:10.1029/94JB02128.

Hirth, G., and D. Kohlstedt (1995b), Experimental constraints on the dynamics of partially molten upper mantle: Deformation in the dislocation creep regime, *J. Geophys. Res.*, *100*, 15,411–15,450.

Hirth, G., and D. Kohlstedt (2003), Rheology of the upper mantle and the mantle wedge: A view from the Experimentalists, in *Inside the Subduction Factory*, *Geophys. Monogr. Ser*, vol. 138, edited by J. Eiler, pp. 83–105, AGU, Washington, D.C.

Hoernle, K., et al. (2008), Arc-parallel flow in the mantle wedge beneath Costa Rica and Nicaragua, *Nature*, *451*, 1094–1097, doi:10.1038/nature06550.

Honda, S. (1985), Thermal structure beneath Tohoku, Northeast Japan–A case study for understanding the detailed thermal structure of the subduction zone, *Tectonophysics*, *112*, 69–102, doi:10.1016/0040-1951(85)90173-8.

Jackson, I., and U. H. Faul (2010), Grain size-sensitive viscoelastic relaxation in olivine: Towards a robust laboratory-based model for seismological application, *Phys. Earth Planet. Inter.*, *183*, 151–163, doi:10.1016/j.pepi.2010.09.005.

Jackson, I., J. D. Fitz Gerald, U. H. Faul, and B. H. Tan (2002), Grain-size sensitive seismic wave attenuation in polycrystalline olivine, *J. Geophys. Res.*, *107*(B12), 2360, doi:10.1029/2001JB001225.

Kaminski, É., and N. M. Ribe (2002), Timescales for the evolution of seismic anisotropy in mantle flow, *Geochem. Geophys. Geosyst.*, *3*(8), 1051, doi:10.1029/2001GC000222.

Karato, S. (1984), Grain-size distribution and rheology of the upper mantle, *Tectonophysics*, *104*, 155–176, doi:10.1016/0040-1951(84)90108-2.

Karato, S. (1989), Grain growth kinetics in olivine aggregates, *Tectonophysics*, *168*, 255–273, doi:10.1016/0040-1951(89)90221-7.

Karato, S. (2003), Mapping water content in the upper mantle, in *Inside the Subduction Factory*, *Geophys. Monogr. Ser.*, vol. 138, edited by J. Eiler, pp. 135–152, AGU, Washington, D.C.

Karato, S., and H. Jung (1998), Water, partial melting and the origin of the seismic low velocity and high attenuation zone in the upper mantle, *Earth Planet. Sci. Lett.*, *157*, 193–207, doi:10.1016/S0012-821X(98)00034-X.

Karato, S., and P. Wu (1993), Rheology of the upper mantle: A synthesis, *Science*, *260*, 771–778, doi:10.1126/science.260.5109.771.

Karato, S., M. Toriumi, and T. Fujii (1980), Dynamic recrystallization of olivine single crystals during high temperature creep, *Geophys. Res. Lett.*, *7*, 649–652, doi:10.1029/GL007i009p00649.

Katayama, I., and S. Karato (2008), Low-temperature, high-stress deformation of olivine under water-saturated conditions, *Phys. Earth Planet. Inter.*, *168*, 125–133, doi:10.1016/j.pepi.2008.05.019.

Kelemen, P. B., J. Rilling, E. M. Parmentier, L. Mehl, and B. R. Hacker (2003), Thermal structure due to solid-state flow in the mantle wedge beneath arcs, in *Inside the Subduction Factory*, *Geophys. Monogr. Ser.*, vol. 138, edited by J. Eiler, pp. 293–311, AGU, Washington, D.C.

Kelley, K. A., T. Plank, T. L. Grove, E. M. Stolper, S. Newman, and E. Hauri (2006), Mantle melting as a function of water content beneath back-arc basins, *J. Geophys. Res.*, *111*, B09208, doi:10.1029/2005JB003732.

Kincaid, C., and I. S. Sacks (1997), Thermal and dynamical evolution of the upper mantle in subduction zones, *J. Geophys. Res.*, *102*, 12,295–12,315, doi:10.1029/96JB03553.

Kneller, E. A., and P. E. van Keken (2008), Effect of three-dimensional slab geometry on deformation in the mantle wedge: Implications for shear wave anisotropy, *Geochem. Geophys. Geosyst.*, *9*, Q01003, doi:10.1029/2007GC001677.

Kopylova, M. G., J. K. Russell, and H. Gookenboo (1999), Petrology of peridotite and pyroxenite xenoliths from the Jericho Kimberlite: Implications fro the thermal state of the mantle beneath the Slave Craton, Northern Canada, *J. Petrol.*, *40*, 79–104, doi:10.1093/petrology/40.1.79.

Lifshitz, I. M., and V. V. Slyozov (1961), The kinetics of precipitation from supersaturated solid solutions, *J. Phys. Chem. Solids*, *19*, 35–50, doi:10.1016/0022-3697(61)90054-3.

Mavko, G. M. (1980), Velocity and attenuation in partially molten rocks, *J. Geophys. Res.*, *85*, 5173–5189, doi:10.1029/JB085iB10p05173.

Montési, L. G., and G. Hirth (2003), Grain size evolution and the rheology of ductile shear zones: From laboratory experiments to postseismic creep, *Earth Planet. Sci. Lett.*, *211*, 97–110, doi:10.1016/S0012-821X(03)00196-1.

Ohuchi, T., and M. Nakamura (2007), Grain growth in the forsterite-diopside system, *Phys. Earth Planet. Inter.*, *160*, 1–21, doi:10.1016/j.pepi.2006.08.003.

Olgaard, D., and B. Evans (1986), Effect of second-phase particles on grain growth in calcite, *J. Am. Ceram. Soc.*, *69*, C272–C277, doi:10.1111/j.1151-2916.1986.tb07374.x.

Piromallo, C., T. W. Becker, F. Funiciello, and C. Faccenna (2006), Three-dimensional instantaneous mantle flow induced by subduction, *Geophys. Res. Lett.*, *33*, L08304, doi:10.1029/2005GL025390.

Plank, T., L. B. Cooper, and C. E. Manning (2009), Emerging geothermometers for estimating slab surface temperatures, *Nat. Geosci.*, *2*, 611–615, doi:10.1038/ngeo614.

Putirka, K. (2008), Excess temperatures at ocean islands: Implications for mantle layering and convection, *Geology*, *36*, 283–286, doi:10.1130/G24615A.1.

Ricard, Y., and D. Bercovici (2009), A continuum theory of grain size evolution and damage, *J. Geophys. Res.*, *114*, B01204, doi:10.1029/2007JB005491.

Riedel, M. R., and S. Karato (1997), Grain-size evolution in subducted oceanic lithosphere associated with the olivine-spinel transformation and its effects on rheology, *Earth Planet. Sci. Lett.*, *148*, 27–43, doi:10.1016/S0012-821X(97)00016-2.

Ross, J. V., H. G. Avé Lallemant, and N. L. Carter (1980), Stress dependence of recrystallized grain and subgrain size in olivine, *Tectonophysics*, *70*, 39–61, doi:10.1016/0040-1951(80)90020-7.

Rychert, C. A., K. M. Fischer, D. G. A. Abers, T. Plank, E. Syracuse, J. M. Protti, V. Gonzalez, and W. Strauch (2008), Strong along-arc variations in attenuation in the mantle wedge beneath Costa Rica and Nicaragua, *Geochem. Geophys. Geosyst.*, *9*, Q10S10, doi:10.1029/2008GC002040.

Schurr, B., G. Asch, A. Rietbrock, R. Trumbull, and C. Haberland (2003), Complex patterns of fluid and melt transport in the central Andean subduction zone revealed by attenuation tomography, *Earth Planet. Sci. Lett.*, *215*, 105–119, doi:10.1016/S0012-821X(03)00441-2.

Solomatov, V.S., R. El-Khozondar, and V. Tikare (2002), Grain size in the lower mantle: Constraints from numerical modeling of grain growth in two-phase systems, *Phys. Earth Planet. Inter.*, *129*, 265–282, doi:10.1016/S0031-9201(01)00295-3.

Stachnik, J. C., G. A. Abers, and D. H. Christensen (2004), Seismic attenuation and mantle wedge temperatures in the Alaska subduction zone, *J. Geophys. Res.*, *109*, B10304, doi:10.1029/2004JB003018.

Stein, C. A., and S. Stein (1992), A model for the global variation in oceanic depth and heat flow with lithospheric age, *Nature*, *359*, 123–129, doi:10.1038/359123a0.

Syracuse, E. M., and G. A. Abers (2006), Global compilation of variations in slab depth beneath arc volcanoes and implications, *Geochem. Geophys. Geosyst.*, *7*, Q05017, doi:10.1029/2005GC001045.

Tamura, Y., Y. Tatsumi, D. Zhao, Y. Kido, and H. Shukuno (2002), Hot fingers in the mantle wedge: New insights into magma genesis in subduction zones, *Earth Planet. Sci. Lett.*, *197*, 105–116, doi:10.1016/S0012-821X(02)00465-X.

Tan, B. H., I. Jackson, and J. D. Fitz Gerald (2001), High-temperature viscoelasticity of fine-grained polycrystalline olivine, *Phys. Chem. Miner.*, *28*, 641–664, doi:10.1007/s002690100189.

Tsumura, N., S. Matsumoto, S. Horiuchi, and A. Hasegawa (2000), Three-dimensional attenuation structure beneath the northeastern Japan arc estimated from spectra of small earthquakes, *Tectonophysics*, *319*, 241–260, doi:10.1016/S0040-1951(99)00297-8.

Twiss, R. J. (1977), Theory and applicability of a recrystallized grain size palaeopiezometer, *Pure Appl. Geophys.*, *115*, 227–244, doi:10.1007/BF01637105.

Urai, J. L., W. D. Means, and C. S. Lister (1986), Dynamic recrystallization of minerals, in *Mineral and Rock Deformation: Laboratory Studies. The Paterson Volume*, *Geophys. Monogr. Ser.*, vol. 36, edited by B. E. H. Hobbs and C. Hugh, AGU, Washington, D.C.

Van der Wal, D., P. Chopra, M. Drury, and I. Fitz Gerald (1993), Relationships between dynamically recrystallized grain size and deformation conditions in experimentally deformed olivine rocks, *Geophys. Res. Lett.*, *20*, 1479–1482, doi:10.1029/93GL01382.

van Keken, P. E., B. Kiefer, and S. M. Peacock (2002), High-resolution models of subduction zones: Implications for mineral dehydration reactions and the transport of water into the deep mantle, *Geochem. Geophys. Geosyst.*, *3*(10), 1056, doi:10.1029/2001GC000256.

Wada, I., and K. Wang (2009), Common depth of decoupling between the subducting slab and mantle wedge: Reconciling diversity and uniformity of subduction zones, *Geochem. Geophys. Geosyst.*, *10*, Q10009, doi:10.1029/2009GC002570.

Wada, I., K. Wang, J. He, and R. D. Hyndman (2008), Weakening of the subduction interface and its effects on surface heat flow, slab dehydration, and mantle wedge serpentinization, *J. Geophys. Res.*, *113*, B04402, doi:10.1029/2007JB005190.

Wang, Z., Q. Bai, G. Dresen, R. Wirth, and B. Evans (1996), High temperature deformation of calcite single crystals, *J. Geophys. Res.*, *101*(B9), 20,377–20,390, doi:10.1029/96JB01186.

Wark, D. A., and E. B. Watson (1998), Grain-scale permeabilities of texturally equilibrated, monomineralic rocks, *Earth Planet. Sci. Lett.*, *164*, 591–605, doi:10.1016/S0012-821X(98)00252-0.

Wark, D. A., C. A. Williams, E. B. Watson, and J. D. Price (2003), Reassessment of pore shapes in microstructurally equilibrated rocks, with implications for permeability of the upper mantle, *J. Geophys. Res.*, *108*(B1), 2050, doi:10.1029/2001JB001575.

Wiens, D. A., J. A. Conder, and U. H. Faul (2008), The seismic structure and dynamics of the mantle wedge, *Annu. Rev. Earth Planet. Sci.*, *36*, 421–455, doi:10.1146/annurev.earth.33.092203.122633.

Zhu, G., T. V. Gerya, D. A. Yuen, S. Honda, T. Yoshida, and J. A. D. Connolly (2009), Three-dimensional dynamics of hydrous thermal-chemical plumes in oceanic subduction zones, *Geochem. Geophys. Geosyst.*, *10*, Q11006, doi:10.1029/2009GC002625.

M. D. Behn and I. Wada, Department of Geology and Geophysics, Woods Hole Oceanographic Institution, 266 Woods Hole Rd., Woods Hole, MA 02543-1050, USA. (iwada@whoi.edu)

J. He, Pacific Geoscience Centre, Geological Survey of Canada, 9860 W Saanich Rd., Sidney, BC V8L 4B2, Canada.